

Boise State University

ScholarWorks

---

Geosciences Faculty Publications and  
Presentations

Department of Geosciences

---

4-2019

## Permeability Prediction in Rocks Experiencing Mineral Precipitation and Dissolution: A Numerical Study

Qifei Niu

*Boise State University*

Chi Zhang

*University of Kansas*

---

This document was originally published in *Water Resources Research* by Wiley on behalf of the American Geophysical Union:

Niu, Q. & Zhang, C. (2019). Permeability Prediction in Rocks Experiencing Mineral Precipitation and Dissolution: A Numerical Study. *Water Resources Research*, 55(4), 3107-3121. <https://doi.org/10.1029/2018WR024174>

Copyright restrictions may apply.

# Water Resources Research

## RESEARCH ARTICLE

10.1029/2018WR024174

### Key Points:

- Fluid and electric flows are numerically simulated at the pore scale in rocks undergoing precipitation and dissolution
- Simulations show that rock permeability  $k$  can be fairly well estimated with the electrical tortuosity and an appropriate length scale
- The uncertainty of the  $k$  prediction is mainly from the electrical tortuosity, which can underestimate the true hydraulic tortuosity

### Correspondence to:

C. Zhang,  
chizhang@ku.edu

### Citation:

Niu, Q., & Zhang, C. (2019). Permeability prediction in rocks experiencing mineral precipitation and dissolution: A numerical study. *Water Resources Research*, 55, 3107–3121. <https://doi.org/10.1029/2018WR024174>



Received 25 SEP 2018

Accepted 23 MAR 2019

Accepted article online 1 APR 2019

Published online 15 APR 2019

## Permeability Prediction in Rocks Experiencing Mineral Precipitation and Dissolution: A Numerical Study

Qifei Niu<sup>1,2</sup>  and Chi Zhang<sup>1</sup> 

<sup>1</sup>Department of Geology, The University of Kansas, Lawrence, KS, USA, <sup>2</sup>Now at Department of Geosciences, Boise State University, Boise, ID, USA

**Abstract** In this study, we focus on the electrical tortuosity-based permeability model  $k = r_{\text{eff}}^2/8F$  ( $r_{\text{eff}}$  is an effective pore size, and  $F$  is the formation factor) and analyze its applicability to rocks experiencing mineral precipitation and dissolution. Two limiting cases of advection-dominated water-rock reactions are simulated, that is, the reaction-limited and transport-limited cases. At the pore scale, the two precipitation/dissolution patterns are simulated with a geometrical model and a phenomenological model. The fluid and electric flows in the rocks are simulated by directly solving the linear Stokes equation and Laplace equation on the representative elementary volume of the samples. The numerical results show that evolutions of  $k$  and  $F$  differ significantly in the two limiting cases. In general, the reaction-limited precipitation/dissolution would result in a smooth variation of  $k$  and  $F$ , which can be roughly modeled with a power function of porosity  $\phi$  with a constant exponent. In contrast, the transport-limited precipitation/dissolution mostly occurs near the pore throats where the fluid velocity is high. This induces a sharp change in  $k$  and  $F$  despite a minor variation in  $\phi$ . The commonly used power laws with constant exponents are not able to describe such variations. The results also reveal that the electrical tortuosity-based permeability prediction generally works well for rocks experiencing precipitation/dissolution if  $r_{\text{eff}}$  can be appropriately estimated, for example, with the electrical field normalized pore size  $\Lambda$ . The associated prediction errors are mainly due to the use of electrical tortuosity, which might be considerably larger than the true hydraulic tortuosity.

### 1. Introduction

In hydrology and many water-related disciplines, the distribution of permeability  $k$  in the subsurface is crucial for conducting a flow analysis, for example, to assess the aquifer performance under different water usage scenarios (Paniconi & Putti, 2015), to predict the organic solute plume front in contaminated sites (e.g., Rizzo & de Barros, 2017), and to evaluate different waterflooding strategies to recovery additional oils from reservoirs (e.g., Friesen et al., 2017). The permeability of a rock is primarily controlled by its texture (e.g., porosity, particle/pore size, sorting, and surface area) and mineralogy, and it can vary over several orders of magnitude (e.g., Brace, 1980) owing to the heterogeneous nature of the rock (Honarpour et al., 1995). In the last several decades, there has been a continuous effort to explore the links between  $k$  and the rock's texture (and/or mineralogy; e.g., Bryant & Blunt, 1992; Garboczi, 1990; Kwon et al., 2004; Mualem, 1976; Xu & Yu, 2008). These studies have significantly improved our capability of predicting a rock's permeability to understand the fluid flow phenomenon in the subsurface.

From a geological viewpoint, the permeability of a rock is not stationary but continuously evolves during diagenesis. This is because diagenetic processes, for example, compaction, mineral precipitation/dissolution, and weathering, can significantly alter a rock's texture and mineralogy, resulting in the change in  $k$  (Cardell et al., 2008; Noiriél et al., 2004; Popp et al., 2001). To better understand the fluid flow phenomenon in rocks, it is therefore necessary to analyze how diageneses affect a rock's microstructure and thus its permeability. Such analysis is an area of interest for studying many geological systems and processes, such as crustal hydrothermal systems (Steeffel & Lasaga, 1994), fluid flow in Earth's mantle (Kelemen et al., 1995), and saline water circulating in carbonates (Whitaker & Smart, 1997). In particular, these analyses are critical for carbonate rocks, of which the permeability-porosity relations do not follow the trend observed in sandstones (e.g., Ehrenberg & Nadeau, 2005) due to more severe precipitation and (or) dissolution. From a practical perspective, the knowledge of diagenetic influences on  $k$ , especially

those related to mineral precipitation and dissolution, could benefit many engineering projects such as geological CO<sub>2</sub> sequestration (Luquot & Gouze, 2009), bioremediation and soil improvement with microbially induced calcite precipitation (Achal et al., 2011; Montoya & DeJong, 2015), and oil recovery by injecting acid in reservoirs (Emberley et al., 2004).

To date, there have been many studies on the microstructural and permeability variations of rocks during mineral precipitation and/or dissolution (e.g., see a recent study in Luhmann et al., 2017, and the references therein). These studies can be grouped into two categories: laboratory experiments and pore-scale numerical simulations. Most laboratory experiments are conducted under controlled flow and environmental conditions (e.g., Garcia-Rios et al., 2015), and the samples are characterized in detail with advanced pore-scale imaging techniques (Noiriel, 2015). These experiments provide valuable data for us to understand different precipitation/dissolution patterns in rocks and their controlling factors. As an alternative, a pore-scale numerical simulation has also been widely used in studying the effect of precipitation/dissolution on rock properties (e.g., Miller et al., 2017; Molins et al., 2017; Qin et al., 2016; Yoon et al., 2012). One advantage of numerical simulations is that many microscopic parameters of rocks, which are difficult to determine in experiments, can be directly extracted from the digital representation of the microstructure of the samples (Blunt et al., 2013). Another advantage is that different precipitation/dissolution patterns (e.g., uniform dissolution versus wormholing; Golfer et al., 2002) can be relatively easily controlled in the simulation (e.g., Jiang & Tsuji, 2014). Currently, the main focus of pore-scale simulations is still on developing microscale precipitation/dissolution models that can reproduce the variations in a rock's microstructure and bulk properties as observed in laboratory experiments (e.g., Miller et al., 2017; Nunes et al., 2016).

One of the most important goals in studying rocks experiencing precipitation and/or dissolution is to develop a predictive  $k$  model. Currently, a large body of the relevant research centers on empirical porosity-permeability models such as the power law model and Kozeny-Carman equation (e.g., Bernabé et al., 2003; Zhu et al., 2007). The general conclusion from these studies is that the model parameter(s) varies considerably during the diagenetic processes. Therefore, the permeability predictions from these empirical relations with fixed model parameters are not satisfactory. Recently, attempts have been made to incorporate diagenetic processes in the Kozeny-Carman equation (e.g., Ghezzehei, 2012), and these process-based studies have provided valuable, pore-scale insights into the diagenetic controls on rock's permeability.

At laboratory scales, the permeability of rocks can also be estimated with the aid of geophysical data such as electrical resistivity (Revil & Cathles, 1999; Slater & Lesmes, 2002), induced polarization (Binley et al., 2005; Revil et al., 2015), and nuclear magnetic resonance (NMR) relaxation (Daigle & Dugan, 2011; Kenyon et al., 1988). The underlying principle of these applications is the use of geophysical parameters (i.e., formation factor, imaginary conductivity, induced polarization relaxation frequency, and NMR  $T_2$  relaxation time) to estimate the hydraulic tortuosity (Duda et al., 2011) or the effective pore radius. By doing so, the permeability of the rock can then be estimated from a simple torturous bundle of capillary tubes model (e.g., Cai et al., 2014) without knowing the detailed rock texture (see detailed discussions in section 2). Due to the noninvasive nature and applicability in field tests, predicting permeability from geophysical data could potentially be a useful means to determine the spatial hydraulic heterogeneity in field scales (e.g., Maurya et al., 2018) if the lab-derived petrophysical relations can be properly upscaled to field scales. Despite the existence of many geophysical-based  $k$  prediction models (see Binley et al., 2015), it is, however, unclear whether they still hold for rocks experiencing different patterns of precipitation or dissolution.

This study aims to understand whether the commonly used, electrical tortuosity-based permeability model,  $k = r_{\text{eff}}^2/8F$  ( $r_{\text{eff}}$  is an effective pore size, and  $F$  is the formation factor; e.g., see Avellaneda & Torquato, 1991), still works for rocks in different mineral precipitation/dissolution scenarios using a pore-scale, numerical approach. In section 2, the theoretical background of the permeability model is reviewed. Section 3 describes the details of the pore-scale methods used to simulate precipitation/dissolution, electric current flow, and fluid flow in rocks. The results, including permeability and formation factor, are presented in section 4. In section 5, permeability estimated from  $k = r_{\text{eff}}^2/8F$  is compared with the hydrodynamic calculations and the origins of the prediction errors are also discussed.

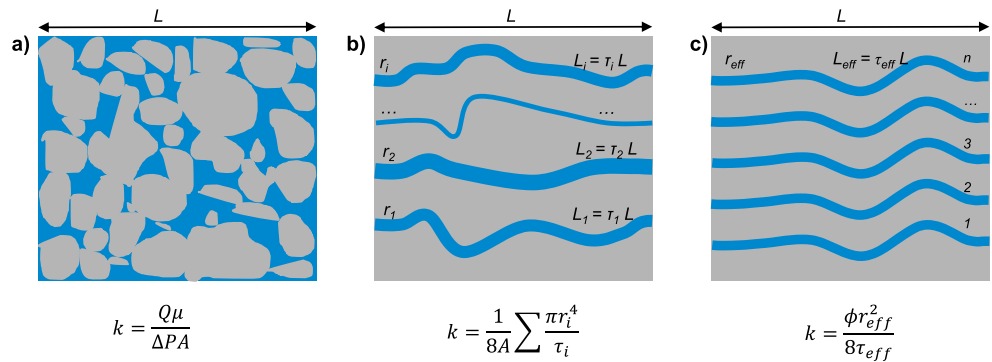


**Figure 1.** Schematics demonstrating different models of a porous rock (pores are indicated in blue, and rock matrix is indicated in gray): (a) a real porous medium, (b) a simplified model consisting of tortuous circular tubes with different size  $r_i$  and length  $L_i$ , and (c) a simplified model having many tortuous circular tubes with same size  $r_{eff}$  and length  $L_{eff}$ . The length of the rock sample is  $L$ , and the related  $k$  expression is also shown in each figure. In Figure 1a, only the connected pores are considered for simplifications. The porosities in Figures 1b and 1c are identical, and they may be less than the actual porosity shown in Figure 1a.

## 2. Permeability Prediction—Theoretical Background

The permeability  $k$  of a porous medium (with a dimensional unit of  $[\text{length}]^2$ ) can be determined experimentally by measuring the flow rate  $Q$  induced by a pressure difference  $\Delta P$  across the sample with Darcy's law (e.g., Lu & Likos, 2004), that is,

$$k = \frac{Q\mu}{\Delta PA}, \quad (1)$$

where  $\mu$  is the viscosity of the fluid and  $A$  is the cross-section area of the sample. According to dimensional analysis, the permeability  $k$  is a product of a squared length scale, that is,  $l^2$ , and a dimensionless and scale-invariant quantity  $H$  (Bernabé et al., 2010):

$$k = Hl^2. \quad (2)$$

Based on equation (2), Bernabé et al. (2010) pointed out that the modeling of  $k$  essentially consists of two steps: (1) the determination of the relevant length scale  $l$  and (2) the selecting of the scale-invariant, dimensionless parameter  $H$ . This viewpoint can be used to understand most, if not all, of the existing permeability prediction models including those incorporating geophysical measurements as will be discussed in details later.

The pore space of a real porous rock usually has a complex structure as shown in Figure 1a, and it is extremely difficult to mathematically describe its geometry (Torquato, 2002). In order to theoretically model the fluid flow, the complex pore space is usually represented by a simplified, equivalent pore space. Here “equivalent” means the permeability of porous media with these two pore spaces is the same. Generally, only connected pores of the rock are considered in the simplification because isolated pores usually do not contribute to the fluid flow. One commonly used model is a bundle of tortuous circular capillary tubes with a dispersed radius  $r_i$  and length  $L_i$  as shown in Figure 1b. In this simplified model, the tubes are in parallel and the fluid flow in each tube can be described by the Hagen-Poiseuille equation. The analytical form of  $k$  for the model in Figure 1b can then be derived as

$$k = \frac{1}{8A} \sum \frac{\pi r_i^4}{\tau_i} \quad (3)$$

where  $\tau_i = \frac{L_i}{L}$  is the tortuosity of tube  $i$  ( $L$  being the length of the sample).

Many permeability models, especially for unsaturated porous media, are based on equation (3), and popular examples include those proposed in Burdine (1953), Mualem (1976), Fredlund et al. (1994), and Kosugi (1996). Note that this type of model needs the pore size  $r_i$  distribution as an input. In practice, the pore size distribution of soils is usually estimated from the water retention curve or particle size distribution, and for rocks, it is usually measured with mercury injection capillary pressure curves. Also, since the tortuosity  $\tau_i$

distribution is not available, the average tortuosity  $\langle \tau_i \rangle$  is commonly used instead of the distribution. In practice,  $\langle \tau_i \rangle$  can be assumed as unity if a bundle of straight capillary tubes model is used (e.g., Kosugi, 1996) or a nonunity constant (e.g.,  $\langle \tau_i \rangle = \sqrt{2}$  for sphere packing in Carman, 1937). More commonly,  $\langle \tau_i \rangle$  is assumed as a function of porosity  $\phi$  (for saturated cases) or water content  $\theta$  (for unsaturated cases); the parameters in these functions are sometimes constrained by texture data (Schuh & Cline, 1990) or geophysical data (e.g., resistivity data; Niu et al., 2015).

The complexity of the pore space in Figure 1b can be further reduced by assuming that  $r_i$  and  $\tau_i$  are constant (i.e., effective radius  $r_{\text{eff}}$  and effective tortuosity  $\tau_{\text{eff}}$  as shown in Figure 1c) and keeping the (connected) porosity unchanged. Similarly, the permeability  $k$  can be determined analytically by applying the Hagen-Poiseuille equation and Darcy's law, expressed as

$$k = \frac{\phi r_{\text{eff}}^2}{8\tau_{\text{eff}}}. \quad (4)$$

In practice, the effective tortuosity  $\tau_{\text{eff}}$  is often estimated from resistivity measurements. Ignoring the surface conduction (Revil & Glover, 1998), the electrical conductivity  $\sigma_{\text{eff}}$  of the sample in Figure 1c is expressed as

$$\sigma_{\text{eff}} = \frac{n\pi r^2}{A\tau_{\text{eff}}} \sigma_f = \frac{\phi}{\tau_{\text{eff}}} \sigma_f, \quad (5)$$

in which  $n$  is the total number of tubes and  $\sigma_f$  is the fluid conductivity. Applying the definition of formation factor  $F = \sigma_f / \sigma_{\text{eff}}$  (Archie, 1942), we can have  $\tau_{\text{eff}} = F\phi$  for the model in Figure 1c. Thus, equation (4) can be rewritten as

$$k = \frac{r_{\text{eff}}^2}{8F}. \quad (6)$$

The above equation is the basis of using resistivity measurements to predict  $k$ . The underlying assumption is that the electrical tortuosity ( $F\phi$ ) is the same as the geometric/hydraulic tortuosity  $\tau_{\text{eff}}$ . In this paper, we term equation (6) as the electrical tortuosity-based permeability model. Compared to the dimensional analysis in equation (2), the term  $1/(8F)$  is then the invariant parameter  $H$ .

Now, the next step is to estimate the effective pore size  $r_{\text{eff}}$  (i.e., the relevant length scale  $l$  in equation (2)). The most common way is to use the hydraulic radius  $r_h$  defined as

$$r_h = \frac{2}{S_{\text{por}}} = \frac{2V}{S}, \quad (7)$$

where  $V$  and  $S$  are respectively the volume and surface area of the pore space and  $S_{\text{por}}$  is the surface area-to-pore volume ratio. Both experimental and theoretical studies have indicated strong links between  $S_{\text{por}}$  and some geophysical responses, such as quadrature conductivity  $\sigma''$  (Binley et al., 2005; Börner, 1992; Weller & Slater, 2015) and NMR  $T_2$  relaxation time (Borgia et al., 1996). This is the reason that  $\sigma''$  and NMR  $T_2$  time have been frequently used to aid the  $k$  prediction in porous media (Daigle & Dugan, 2011; Revil & Florsch, 2010; Weller et al., 2015). Note that other factors may also affect the relations between geophysical responses and  $S_{\text{por}}$ . For instance, the change of salinity and frequency could significantly affect the value of  $\sigma''$  (Weller et al., 2011); the existence of inhomogeneous magnetic field and bulk relaxation could also pose difficulties in interpreting the NMR  $T_2$  relaxation time (Behroozmand et al., 2015).

The dynamic pore size  $\Lambda$  proposed in Johnson et al. (1986) has also been used to estimate  $r_{\text{eff}}$  in  $k$  predictions. For porous media, this parameter describes the effects of the internal surface on many processes such as electrical surface conduction and high-frequency viscous damping of acoustic waves (Johnson et al., 1986). The parameter  $\Lambda$  is defined as

$$\Lambda = \frac{2 \int |\mathbf{E}|^2 dV}{\int |\mathbf{E}|^2 dS}, \quad (8)$$

where  $\mathbf{E}$  is the local electrical field and  $dV$  and  $dS$  denote the integrations are over the pore space and grain-fluid interface, respectively. The  $\Lambda$  parameter is a dynamic length that is determined from the solution of the Laplace equation, and it cannot be measured by a simple geometrical analysis (Kostek et al., 1992). In practice,  $\Lambda$  of a sample can be estimated through experiments, for example, by relating  $\Lambda$  to the characteristic

length scale  $l_c$  (Banavar & Johnson, 1987), which corresponds to the threshold pressure  $p_c$  at which the mercury injection curve starts rapidly rising (Katz & Thompson, 1986).

In pore-scale imaging and modeling, some other pore size parameters are also frequently used, including the pore node/body size  $r_d$  and pore throat size  $r_{th}$  (Lindquist et al., 2000). With the recent advancements in imaging techniques (Wildenschild & Sheppard, 2013), extracting these geometrical parameters from microscopic images becomes readily available, and they have been commonly used to reconstruct the rock structure and to predict the permeability (Blunt et al., 2013).

In summary, equation (6) will be tested in this study with the effective pore size  $r_{eff}$  approximated by four pore size parameters,  $r_h$ ,  $\Lambda$ ,  $r_d$ , and  $r_{th}$ . Then, we have the following four electrical tortuosity-based permeability models to analyze:

$$k = \frac{r_h^2}{8F}, \quad (9a)$$

$$k = \frac{\Lambda^2}{8F}, \quad (9b)$$

$$k = \frac{r_d^2}{8F}, \quad (9c)$$

$$k = \frac{r_{th}^2}{8F}. \quad (9d)$$

### 3. Numerical Methods and Samples

In this section, we introduce the pore-scale, numerical methods used to simulate mineral precipitation/dissolution, fluid flow, and electric current flow in porous media. We also explain briefly how the pore size parameters ( $r_h$ ,  $\Lambda$ ,  $r_d$ , and  $r_{th}$ ) are determined from digital representations of the rock microstructure. These numerical methods are applied on two rock samples, and the properties of the samples are described lastly. Note that all the simulations in this study are performed on three-dimensional samples.

#### 3.1. Precipitation/Dissolution Patterns and Their Modeling

When reactive fluids flow through rocks, due to fluid-rock disequilibrium, chemical reactions such as mineral precipitation/dissolution could happen at the solid-liquid interface (e.g., Morse et al., 2007). This pore-scale chemical reaction could alter a rock's microstructure and thus change the rock's bulk property such as permeability. It is generally believed that the reaction rate is quite heterogeneous within the rock and a number of factors could affect the precipitation/dissolution pattern, including local fluid chemistry, mineralogy, and transport properties (e.g., Molins et al., 2017). Thus, a direct simulation of the precipitation/dissolution at the pore scale (e.g., Nunes et al., 2016) is computationally costly and requires the solution of the advection-diffusion-reaction equation.

Fortunately, the main regimes of precipitation and dissolution have been identified based on experimental and numerical studies (e.g., Golfier et al., 2002; Kang et al., 2003; Nunes et al., 2016), and they can be characterized by the combination of Péclet and Damköhler numbers, that is,  $Pe$  and  $Da$ . The  $Pe$  number compares the rate of advection to the rate of diffusion (e.g., see Kang et al., 2003), and it can be defined as  $Pe = uL_c/D_m$  where  $u$  and  $L_c$  respectively are characteristic Darcy velocity and length of the system and  $D_m$  is the diffusion coefficient. The  $Da$  number is defined as the ratio of advective time over reaction time (e.g., Nunes et al., 2016), that is,  $Da = k_r/u$ , where  $k_r$  is the local reaction rate. In this study, we use simplified models to mimic the precipitation and dissolution at the pore scale, aiming to capture the main macroscopic features of the samples as observed in laboratory experiments. In the simulation, the fluid transport is assumed as advection dominated, that is,  $Pe > 1$ . Under this transport condition, two limiting cases will be considered (Nunes et al., 2016): (1) the transport-limited case, in which the reaction at the solid-liquid interface is limited by the diffusion of reactants to and from solid surfaces, that is,  $PeDa < 1$ ; and (2) the

reaction-limited case, in which the reaction is limited by the reaction rate at the solid-liquid interface (i.e.,  $PeDa > 1$ ). In carbonate dissolution, the transport-limited case is typically related to the “wormholing,” while the reaction-limited case generally corresponds to the so-called uniform dissolution phenomena (Golfier et al., 2002).

As observed in laboratory experiments, the reaction-limited precipitation/dissolution pattern (defined at the sample scale) is characterized by a roughly uniform growth/removal of minerals at the solid-liquid interface (e.g., Noiriél et al., 2016). Here we use a geometry-based model to simulate the reaction-limited precipitation and dissolution. This model is adopted from the random growth model used in Noiriél et al. (2016) to simulate crystal growth on aragonite grains. The mineral crystals are added (in precipitation) or removed (in dissolution) through a series of discrete steps, and the following summarizes the procedures to realize it in our simulations. First, the voxels at the solid-liquid interface are identified, and this can be done by tracing the phase connectivity to identify a phase change (e.g., see Zhan et al., 2010). In precipitation, these voxels are within the pore space; in dissolution, they are in solid phases. Second, we convert the binary microstructure into a porosity field. By doing this, a continuous growth/erosion of the pore wall can be realized later (Miller et al., 2017). During a time step  $\Delta t$ , the porosity of the interface voxels is updated by a porosity change of  $\Delta\theta < 1$  (i.e., the porosity of the voxel is decreased by  $\Delta\theta$  in precipitation or increased by  $\Delta\theta$  in dissolution), and the locations of the updated voxels are randomly selected following a uniform distribution with a possibility of  $p$ . These two steps are repeated to mimic the heterogeneous mineral precipitation/dissolution at the pore scale. In this process, if the porosity of an interface voxel reaches 0 (in precipitation) or 1 (in dissolution), the phase of the voxels is then converted. The above steps are repeated on the discretized rocks until the target porosity is reached.

Different from the reaction-limited process, the transported-limited (advection-dominated) precipitation and dissolution are even more heterogeneous at the pore scale (e.g., Ott & Oedai, 2015) because the reaction is constrained by the availability of reactants transported to or from the interface, which are related to the local flow conditions. In this study, we use the strategy proposed in Miller et al. (2017) to simulate this limiting case. The method assumes the local fluid velocity field is a proxy of the solvent flux, and it is equivalent to solving the zeroth-order rate equation at the solid-liquid interface (Miller et al., 2017). Overall, the numerical realization is similar to that of the reaction-limited case except that the amount of local porosity change  $\Delta\theta$  during  $\Delta t$  is not a constant but scaled by  $v_m/v_{\max}$ , where  $v_m$  is the local average fluid velocity (e.g., five-voxel neighborhood) and  $v_{\max}$  is the maximum fluid velocity in the pore space. In the simulation, the fluid velocity field of the sample is determined by solving the linear Stokes equation (see section 3.2). As the pore space is continuously altered by mineral precipitation/dissolution, the fluid velocity field in the pore space in our simulation is also updated in the processes.

### 3.2. Fluid and Electric Current Flow Simulations

To determine the fluid velocity field in the pore space of the sample, the linear Stokes equation is numerically solved. In the calculation, we use the Stokes solver developed at the National Institute of Standards and Technology (Garboczi, 1998). After applying a potential gradient across the sample, the code solves the spatial distribution of the pressure and fluid velocity using a staggered-grid finite difference scheme. The permeability  $k$  of the sample can then be determined by applying Darcy's law based on the averaged fluid velocity (e.g., Zhan et al., 2010). The Stokes solver is written in FORTRAN, and the preprocessing code is written in C. For a sample with  $300^3$  voxels, the calculation usually takes about 1 to 3 hr on a personal computer depending on the complexity of the model.

The electric flow in the sample is simulated using the finite difference code DC3d developed in the National Institute of Standards and Technology (Garboczi, 1998). In the simulation, the pore fluid conductivity  $\sigma_f$  is kept unchanged during the mineral precipitation/dissolution. The solid phase is assumed to have a uniform material property, and its electrical conductivity is zero. The conduction contributed from the electrical double layer at the solid-liquid interface (i.e., surface conduction; Revil & Glover, 1998) is ignored, and thus, no extra conductivity is added to either fluid or solid phase in the calculation (Niu & Zhang, 2017). The assumption of zero surface conductivity corresponds to rocks at the high-salinity limit where the conduction from bulk fluid is much higher than the surface conduction. It is noted the (intrinsic) formation factor  $F$  is an intrinsic rock property, which is independent of the fluid and solid-liquid interface properties (e.g., see equation 7a in Schwartz et al., 1989). The code applies a uniform electric field across the sample and then solves

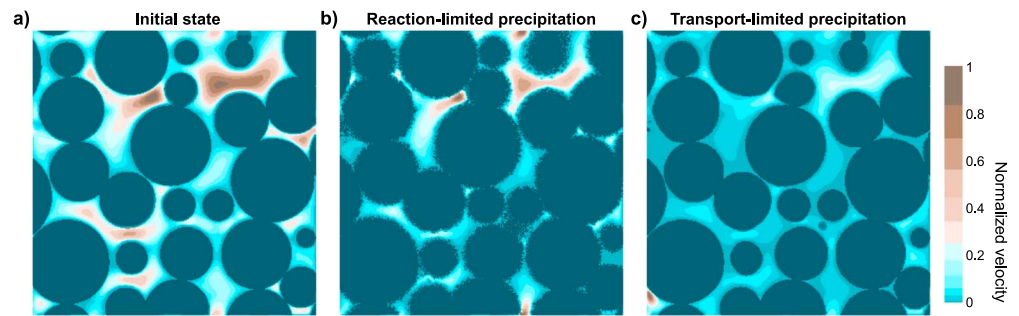


**Figure 2.** Microstructure and fluid velocity field of Sample 1: (a) initial condition ( $\phi = 30.2\%$ ), (b) after reaction-limited precipitation ( $\phi = 20.1\%$ ), and (c) after transport-limited precipitation ( $\phi = 28.2\%$ ). The solid phase is indicated in dark blue. The fluid velocity is normalized by the maximum flow velocity in the pore space. The resolution of the images (size of each voxel) is  $\sim 4.3 \mu\text{m}$ , and the sample volume is  $300^3$  voxels.

the spatial electric potential and current density in the sample with the conjugate gradient method. Based on averaged current density, Ohm's law can be used to calculate the effective electrical conductivity of the sample  $\sigma_{\text{eff}}$  (e.g., Niu & Zhang, 2018). Since  $\sigma_{\text{eff}}$  is solely from the ionic conduction in the bulk solution, the formation factor  $F$  of the sample can be simply determined as  $F = \sigma_f / \sigma_{\text{eff}}$ . The code is also written in FORTRAN, and the calculation time usually is shorter than that of the Stokes solver.

### 3.3. Calculation of Pore Size Parameters

As defined in equation (7), the hydraulic radius  $r_h$  is related to the surface area  $S$  of the solid-liquid interface and the volume  $V$  of the pore space. In the simulation, the solid-liquid interface of the sample is determined by tracing the phase connectivity (e.g., see Zhan et al., 2010). For each voxel, its six neighbors are checked to identify the phase change. If a voxel is isolated with zero connectivity, we simply eliminate it. After the interface is identified,  $V$  and  $S$  can then be easily determined, and then  $r_h$  can be calculated. The determination of  $\Lambda$  is similar to that of  $r_h$ , but the weighting of each voxel is not unity but dependent on the electrical field  $|\mathbf{E}|^2$  according to equation (8). The electrical field  $\mathbf{E}$  is the gradient of the electrical potential field, which is the solution of the Laplace equation.

As discussed, the mean pore node size  $r_d$  and pore throat size  $r_{th}$  are only related to the geometry of the pore space, and they can be determined using the concept of maximum balls (e.g., Al-Kharusi & Blunt, 2007) or by medial axis analysis of the pore space (e.g., Lindquist et al., 1996). In this study, we use the modified maximal ball algorithm developed by Dong and Blunt (2009) to determine the distribution of the pore node size and pore throat size. This two-step algorithm searches the nearest solid to define a void ball, and it defines pore nodes and pore throats by affiliating the maximal balls into family trees according to their size and rank (Dong & Blunt, 2009). The results are then fitted with a normal distribution to determine the mean value  $r_d$  and  $r_{th}$ .

### 3.4. Samples

Two samples are used in this study: a synthetic loosely packed ooids sample (Sample 1) and a carbonate mudstone (Sample 2). The ooids sample (Figure 2a) with the initial porosity  $\phi = 30.2\%$  is obtained using the discrete element method by compressing sparsely distributed spherical particles (e.g., Niu & Zhang, 2018). The carbonate mudstone sample has a porosity of  $\sim 13\%$  (from helium measurement) and is from the Wellington Formation, KS; its microstructural image in Figure 3a is from micro-computed tomography scan data after segmentation. In this study, Sample 1 (Figure 2a) is used for precipitation simulations and Sample 2 (Figure 3a) is used for dissolution simulations.

## 4. Simulation Results of Fluid and Electric Current Flows

The limiting scenarios of precipitation and dissolution are numerically simulated using the methods mentioned above for Samples 1 and 2, respectively. Their permeability  $k$  and formation factor  $F$  are also calculated during the precipitation and dissolution, and the results are shown in Figures 4 and 5. To facilitate



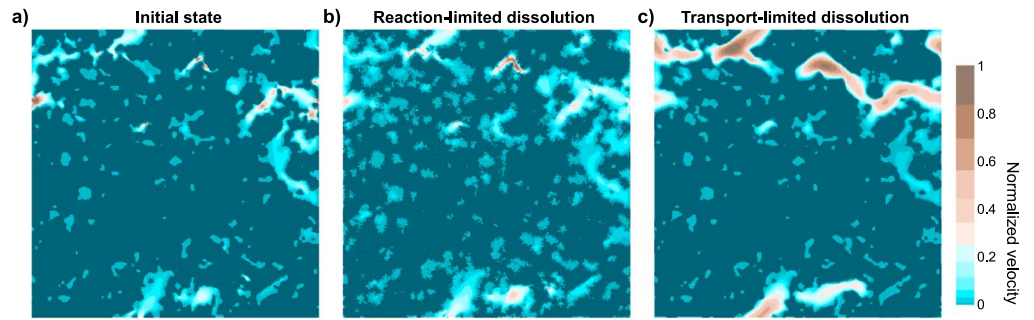


**Figure 3.** Microstructure and fluid velocity field of Sample 2: (a) initial state ( $\phi = 13.8\%$ ), (b) after reaction-limited dissolution ( $\phi = 28.8\%$ ), and (c) after transport-limited dissolution ( $\phi = 17.1\%$ ). The solid phase is indicated in dark blue. The fluid velocity is normalized by the maximum flow velocity in the pore space. The resolution of the images (size of each voxel) is  $\sim 4.3 \mu\text{m}$ , and the sample volume is  $300^3$  voxels.

the discussion, we also plot the empirical power law of  $k$  (e.g., Zhu et al., 2007) and Archie's law (Archie, 1942) with varying model parameters in the figures. The two models are expressed as

$$\frac{k}{k_0} = \left(\frac{\phi}{\phi_0}\right)^n \quad (10)$$

and

$$F = \phi^{-m}, \quad (11)$$

where  $k_0$  is the permeability of the sample at the initial porosity  $\phi_0$ , the exponent  $n$  is an empirical constant, and Archie's porosity exponent  $m$  is usually called cementation factor. The  $k$ - $\phi$  and  $F$ - $\phi$  relations of rocks have been extensively studied with laboratory experiments (e.g., Bernard et al., 2007; Noiriel et al., 2004). In the following, we discuss whether our simulated  $k$  and  $F$  show similar trends as those in published studies and analyze their associated microstructural variations.

#### 4.1. Precipitation (Sample 1)

In simulating the reaction-limited precipitation, the porosity change ( $\Delta\theta$ ) of a voxel during a time step  $\Delta t$  is set as 0.5, and only 5% of the interface voxels are allowed to change phase; a total of 100 time steps are simulated in the calculation, and this induces a porosity reduction of  $\sim 10\%$ , from  $\sim 30.2\%$  to  $\sim 20.1\%$  (Figure 4b). In simulating the transport-limited precipitation, the maximum  $\Delta\theta$  value is 0.3, and 200 time steps are considered in the simulation; the resulted porosity decrease is insignificant, only  $\sim 2\%$  as shown in Figure 4b.

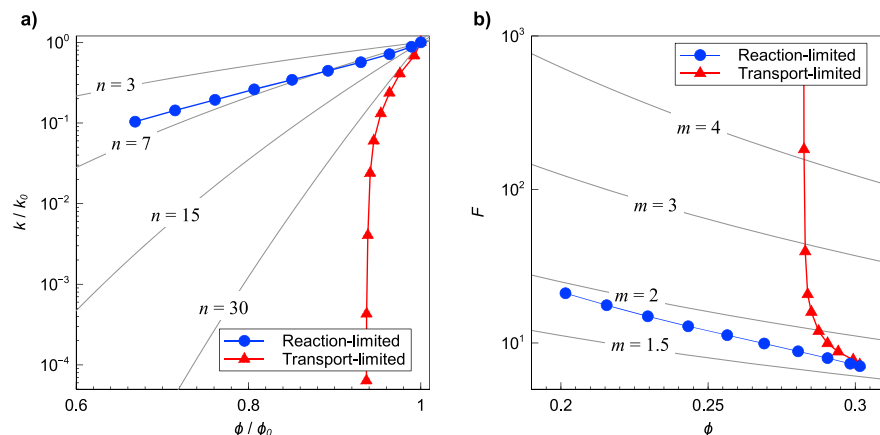


**Figure 4.** Simulation results of Sample 1: (a)  $k$  evolution and (b)  $F$  evolution during reaction-limited and transport-limited precipitation. The parameters  $n$  and  $m$  are the exponents in  $k/k_0 = (\phi/\phi_0)^n$  and  $F = \phi^{-m}$  (i.e., equations (10) and (11)).

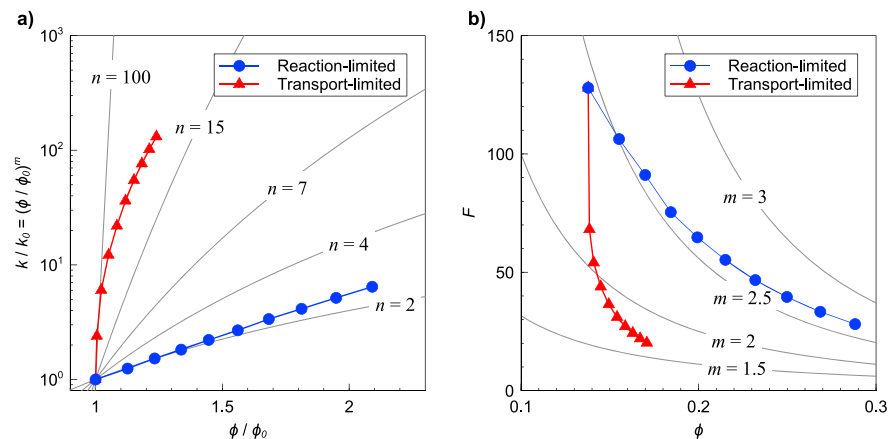


**Figure 5.** Simulation results of Sample 2: (a) permeability  $k$  evolution and (b)  $F$  evolution during reaction-limited and transport-limited dissolution. The parameters  $n$  and  $m$  are the exponents in  $k/k_0 = (\phi/\phi_0)^n$  and  $F = \phi^{-m}$  (i.e., equations (10) and (11)).

The simulated  $k$ - $\phi$  and  $F$ - $\phi$  relations are quite different for the two precipitation. For reaction-limited case (blue symbols in Figure 4), both exponents ( $n$  and  $m$ ) are almost constant without a large variation. For example, in the entire porosity range,  $n$  is close to  $\sim 5$ , while  $m$  is roughly between 1.5 and 2. The microstructure of the sample after the reaction-limited precipitation is shown in Figure 2b, and it appears that, at the sample scale, the precipitated minerals uniformly distribute on the grain surface. These numerical features are consistent with those observed in high-porosity Fontainebleau sandstones (Bourbie & Zinszner, 1985) where the uniform silica overgrowth induces an insignificant variation in  $n$  and  $m$  (Gomez et al., 2010; Revil et al., 2014). It seems that the uniformly precipitated minerals did not significantly change the electric/fluid flow patterns in the pore space (e.g., see Figures 2a and 2b) and that the reaction-limited precipitation may be characterized by a constant porosity exponent  $n$  (or  $m$ ).

For transport-limited cases in Figure 4 (red symbols), both exponents varied considerably despite the minor porosity reduction. For instance,  $n$  quickly exceeds  $\sim 30$  after a porosity decrease of  $\sim 2\%$ , and  $m$  lastly reaches  $\sim 5.1$  when  $\phi = 28\%$ . The increased  $m$  and  $n$  in transport-limited precipitation are associated with the fact that the precipitated minerals accumulate mostly near the pore throats where fluid velocity is relatively high (see Figures 2a and 2c). These numerical results agree with the experimental observations in many published studies (e.g., see Noiriel et al., 2004; Leroy et al., 2017). Thus, it is clear that the transport-limited precipitation has a profound influence on the fluid/electric flow, and it may be characterized by a sharply increased  $n$  (or  $m$ ).

#### 4.2. Dissolution (Sample 2)

The same parameters (e.g.,  $\Delta t$ ,  $\Delta \theta$ , and time step) were used to simulate mineral dissolution in Sample 2, and the calculated  $k$  and  $F$  are shown in Figure 5. For reaction-limited dissolution (blue symbols), both  $k/k_0$  and  $F$  are power functions of porosity  $\phi$  with constant exponents, for example,  $n = \sim 2$  in Figure 5a and  $m = \sim 2.5$  in Figure 5b. In transport-limited cases (red symbols), however, the associated exponents ( $n$  and  $m$ ) vary largely. For instance, the porosity exponent  $n$  decreases from  $\sim 100$  at  $\phi = 13.8\%$  to  $\sim 20$  at  $\phi = 17.1\%$ . This huge decrease in  $n$  has been experimentally observed in limestones where a  $\sim 2\%$  porosity increase causes  $n$  to change from  $\sim 150$  to  $\sim 15$  (Noiriel et al., 2004). The microstructural variations of the sample (Figure 3) are also quite similar to those of Sample 1 (Figure 2). While in reaction-limited dissolution, the dissolved minerals are almost uniformly distributed on all the solid-liquid interface (Figure 3b), the transport-limited dissolution mainly occurs in some preferred channels (Figure 3c) where the fluid velocity is high (Figure 3a). For both dissolution, the porosity exponent  $n$  and  $m$  can be used to characterize the microstructural variations in rocks.

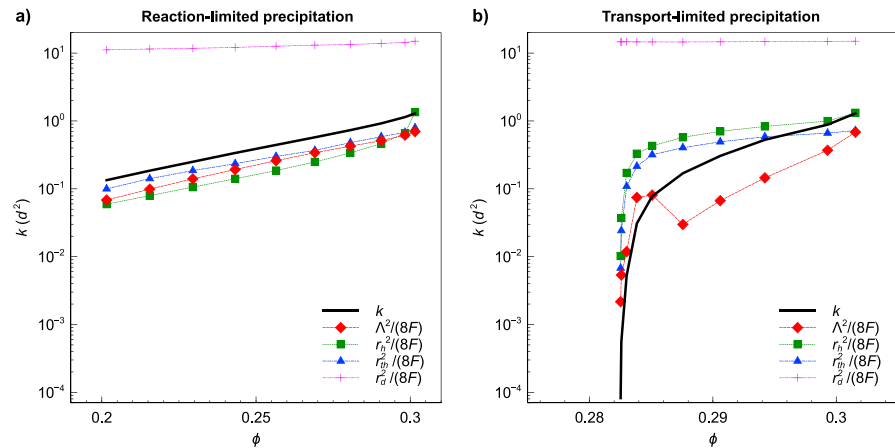


**Figure 6.** The predicted permeability of Sample 1 during (a) reaction-limited precipitation and (b) transport-limited precipitation. The unit of permeability  $k$  is in  $d^2$ , where  $d$  is the voxel size.

### 5. Permeability Predictions

In this section, we compare the  $k$  predictions to their true values for the two samples undergoing different patterns of precipitation/dissolution. We also discuss the origin of the prediction errors in each scenario. Note that our focus here is the sample's permeability in response to pore-scale precipitation/dissolution, and the results need to be upscaled to field scales for hydrogeological applications. Currently, the upscaling of lab-based, hydrogeophysical relations still remain as an unsolved problem in hydrogeology.

#### 5.1. Permeability Predictions

The permeability predicted with (9a) is shown in Figures 6 and 7 for the two samples under different types of precipitation/dissolution. Four pore size parameters were used in the predictions, and they are  $\Lambda$ ,  $r_h$ ,  $r_{th}$ , and  $r_d$ . The permeability determined from hydrodynamic calculations, that is, solving the linear Stokes equation, is also shown for comparison. In Figures 6 and 7, one major finding is that the prediction from the pore body size  $r_d$  significantly overestimates the permeability,  $\sim 2$  orders, for all the cases. This is understandable because it is the pore throat rather than pore body that controls the fluid flow in porous media.

For reaction-limited cases (Figures 6a and 7a), parameters  $\Lambda$ ,  $r_h$ , and  $r_{th}$  give very good permeability estimates, and in general, the discrepancies are less than a half order. In contrast, in transport-limited cases (Figures 6b and 7b), all the predictions deviate noticeably from the true permeability. Among them, the pore size  $\Lambda$  still gives a fair  $k$  estimation, and the associated discrepancy is roughly  $\sim 0.5$  order (e.g., Figure 7b).

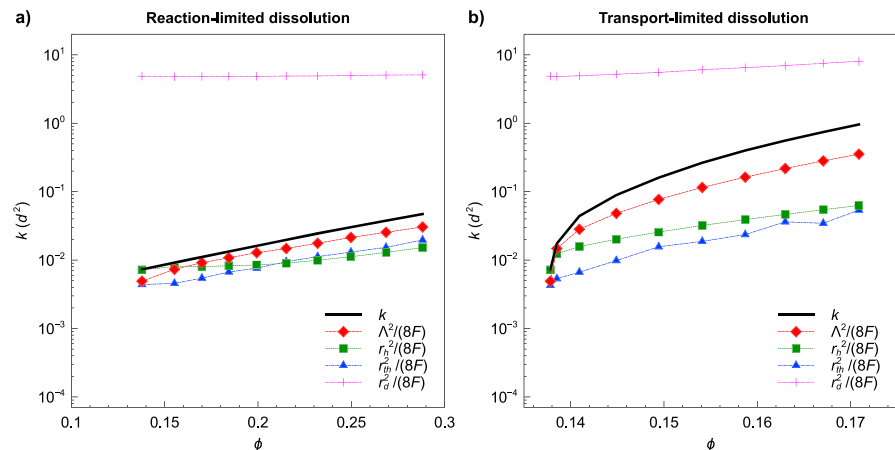


**Figure 7.** The predicted permeability of Sample 2 during (a) reaction-limited dissolution and (b) transport-limited dissolution. The unit of permeability  $k$  is in  $d^2$ , where  $d$  is the voxel size.

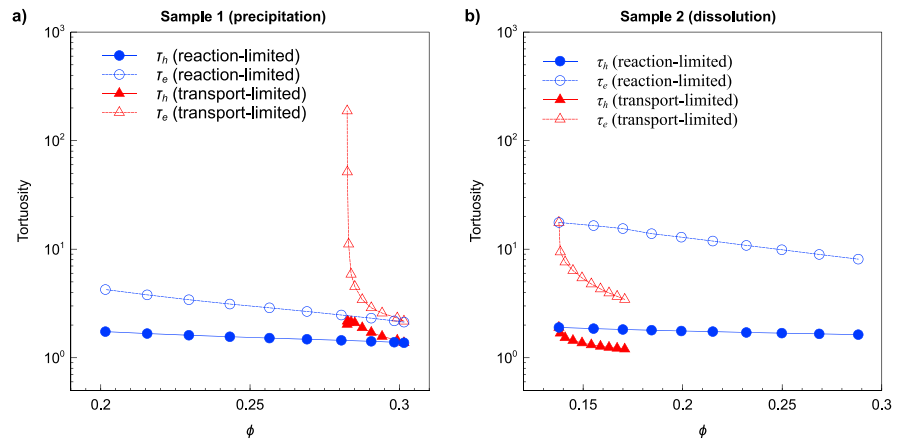


**Figure 8.** Evolutions of electrical tortuosity  $\tau_e$  and hydraulic tortuosity  $\tau_h$  during (a) precipitation (Sample 1) and (b) dissolution (Sample 2).

This indicates that the applicability of the electrical tortuosity-based permeability ((9a)) largely depends on the patterns of the mineral precipitation and dissolution. It seems the electrical tortuosity-based  $k$  prediction works better for rocks experiencing reaction-limited precipitation and dissolution where the mineral growth and removal are roughly uniformly distributed on the solid-liquid interface. Among these pore size parameters, the electrical field normalized pore size  $\Lambda$  works fairly well for both reaction- and transport-limited cases.

### 5.2. Discussion on the Origin of $k$ Prediction Errors

According to equations (4) and (6), the uncertainty of  $k$  predictions may come from two sources: (1) the length scale  $r_{\text{eff}}$  estimation and (2) the tortuosity  $\tau_{\text{eff}}$  estimation. In equation (6), while different pore size parameters ( $\Lambda$ ,  $r_h$ ,  $r_{\text{th}}$ , and  $r_d$ ) are used to estimate  $r_{\text{eff}}$ , the tortuosity is estimated by the electrical tortuosity  $\tau_e = F\phi$ . In the following, we compare the electrical tortuosity  $\tau_e$  to the true tortuosity, that is, the hydraulic tortuosity  $\tau_h$ , which can be determined from the fluid velocity field, expressed as (Duda et al., 2011)

$$\tau_h = \frac{\langle v_{\text{mag}} \rangle}{\langle v_{\parallel} \rangle}, \quad (12)$$

where  $\langle v_{\text{mag}} \rangle$  is the pore volume-averaged fluid velocity magnitude and  $\langle v_{\parallel} \rangle$  is the pore volume-averaged fluid velocity parallel to the applied pressure gradient.

The tortuosity of Samples 1 and 2 is presented in Figures 8a and 8b, respectively. It is shown that for both samples, the calculated electrical tortuosity  $\tau_e$  (empty symbols) is larger than the hydraulic tortuosity  $\tau_h$  (solid symbols) in all the scenarios. In Figure 8, the ratio  $\tau_e/\tau_h$  is roughly  $\sim 3$  for Sample 1 and  $\sim 10$  for Sample 2. They correspond to an underestimation of  $k$  of  $\sim 0.3$  and  $\sim 1$  order. These magnitudes are in accordance with the discrepancies between predicted and true permeability as observed in Figures 6 and 7. This implies that using  $F\phi$  to represent  $\tau_{\text{eff}}$  could underestimate the permeability significantly. Moreover, in reaction-limited cases (blue symbols), both hydraulic and electrical tortuosity changes smoothly. In contrast, the tortuosity in transport-limited cases (red symbols) varies considerably despite the minor porosity change. These distinct responses may be associated with the different microstructural variations as discussed before (e.g., a relatively uniform change of the solid-liquid interface in Figures 2b and 3b and an increased mineral growth/removal near the main flow paths in Figures 2c and 3c).

Now we analyze the accuracy of using  $\Lambda$ ,  $r_h$ ,  $r_{\text{th}}$ , and  $r_d$  to estimate the effective pore size  $r_{\text{eff}}$  in calculating  $k$  (equation (4)). We calculate the true  $r_{\text{eff}}$  value from the true permeability  $k$  and hydraulic tortuosity  $\tau_h$ , expressed as

$$r_{\text{eff}} = \sqrt{\frac{8k\tau_h}{\phi}}. \quad (13)$$

The evolutions of these pore size parameters are shown in Figures 9 and 10 for Sample 1 (precipitation) and Sample 2 (dissolution), respectively. In Figures 9a and 10a, it appears that  $\Lambda$ ,  $r_h$ , and  $r_{\text{th}}$  are quite close to  $r_{\text{eff}}$ ,

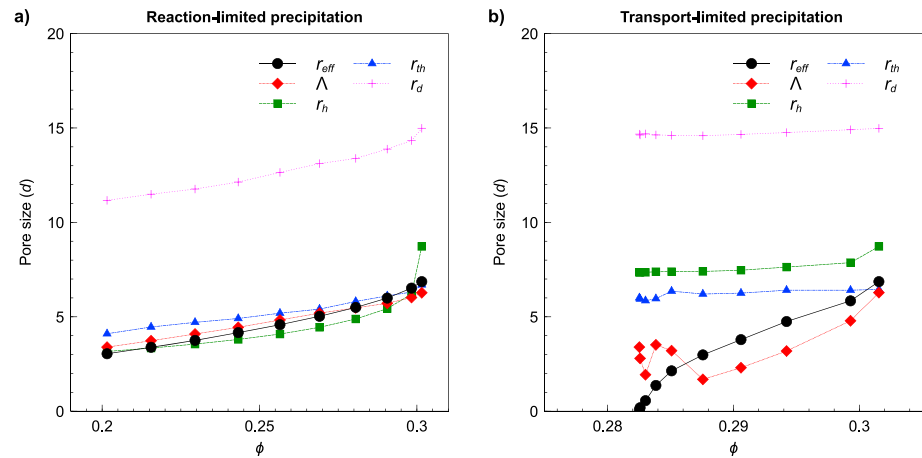


**Figure 9.** Evolutions of different pore size parameters of Sample 1 during (a) reaction-limited precipitation and (b) transport-limited precipitation.

indicating that the length scale controlling fluid flow can be safely estimated by any of them for reaction-limited precipitation/dissolution. This also confirms that the errors of  $k$  predictions in Figures 6a and 7a are mainly from the tortuosity estimation. In transport-limited cases, pore size parameters such as  $r_h$  and  $r_{th}$  cannot capture the significant variations of the effective pore size constraining the fluid flow, and thus, they have partially contributed to the discrepancies of  $k$  observed in Figures 6b and 7b. If compared with the tortuosity estimation (i.e.,  $F\phi$ ), the contributions of effective pore size estimations are very minor. It is also clear from Figures 9 and 10 that among these four pore size parameters, only  $\Lambda$  can be reliably used to estimate the length scale characterizing the fluid flow in porous media undergoing different types of precipitation and dissolution.

As shown in Figure 9, the calculated electrical tortuosity is always higher than the hydraulic tortuosity. This is because the shear plane (within which the fluid is not moving) is always away from the solid-fluid boundary. Thus, the fluid does not need to move exactly along the rough solid-fluid boundary. In contrast, ions can move within the shear plane. This means the ions near the solid-liquid interface have to move along the rough boundary surface, resulting in a longer flow path than the fluid. Therefore, the electrical tortuosity is higher than the hydraulic tortuosity as shown in Figure 9. The results imply that we have to be very cautious when using electrical tortuosity to approximate hydraulic tortuosity, especially when the internal surface of the rock is very rough.

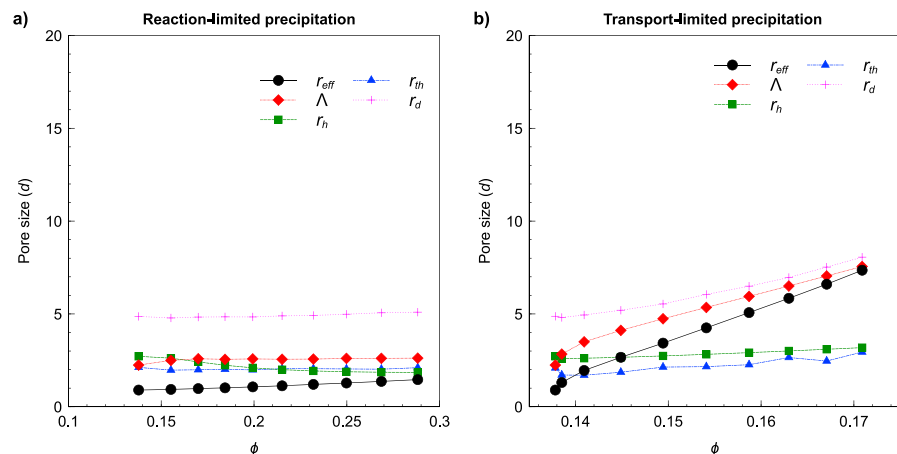


**Figure 10.** Evolutions of different pore size parameters of Sample 2 during (a) reaction-limited dissolution and (b) transport-limited dissolution.

## 6. Conclusions

The pore-scale numerical simulations have shown that the permeability-porosity ( $k$ - $\phi$ ) and formation factor-porosity ( $F$ - $\phi$ ) relations of rocks are largely influenced by the patterns of the mineral precipitation and dissolution. In reaction-limited, advection-dominated cases,  $k$  and  $F$  are roughly power functions of porosity  $\phi$  with the exponents ( $n$  and  $m$ ) nearly constant, and in general, the precipitated or dissolved minerals uniformly distribute at the solid-fluid interface. This microstructural alternation is responsible for the porosity change but did not significantly change the characteristics of the fluid and electric current flows in the pore space. In transport-limited, advection-dominated cases, the precipitated and dissolved minerals are mostly near the pore throats where fluid velocity is relatively high. This heterogeneous microstructural alternation could significantly affect the fluid and electric current flows in the pore space, resulting in a huge change in  $k$  and  $F$  despite a minor variation in  $\phi$ . The commonly used power laws with constant porosity exponents are not able to describe such changes. Compared to reaction-limited cases, transport-limited precipitation/dissolution has a more profound influence on fluid/electric flow and it may be characterized by a sharply changed  $n$  or  $m$ .

In general, the electrical tortuosity-based permeability model  $k = r_{\text{eff}}^2/8F$  works well for rocks experiencing precipitation and dissolution if the effective pore size  $r_{\text{eff}}$  is estimated with the electrical field normalized pore size  $\Lambda$ . The error of the prediction is mainly from the electrically estimated tortuosity, that is,  $F\phi$ , which is consistently larger than the true (hydraulic) tortuosity. In reaction-limited cases, the hydraulic radius  $r_h$  and mean pore throat size  $r_{\text{th}}$  can also be safely used to estimate  $r_{\text{eff}}$ . In all the cases, the pore body size  $r_d$  significantly overestimates the effective pore size, and thus, it should be avoided in permeability predictions of rocks experiencing precipitation and dissolution.

## Acknowledgments

The authors thank Martin Blunt in Imperial College London for providing the pore network extraction code and funding support from Kansas Interdisciplinary Carbonates Consortium. The authors also thank James Colgin II for sharing the micro-CT image of Sample 2. The data used in this paper can be downloaded from <https://doi.org/10.5281/zenodo.2558678>. We thank the Associate Editor and two anonymous reviewers for their constructive comments, which have improved the manuscript significantly.

## References

- Achal, V., Pan, X., & Zhang, D. (2011). Remediation of copper-contaminated soil by *Kocuria flava* CR1, based on microbially induced calcite precipitation. *Ecological Engineering*, *37*(10), 1601–1605. <https://doi.org/10.1016/j.ecoleng.2011.06.008>
- Al-Kharusi, A. S., & Blunt, M. J. (2007). Network extraction from sandstone and carbonate pore space images. *Journal of Petroleum Science and Engineering*, *56*(4), 219–231. <https://doi.org/10.1016/j.petrol.2006.09.003>
- Archie, G. E. (1942). The electrical resistivity log as an aid in determining some reservoir characteristics. *Petroleum Transactions of AIME*, *146*(01), 54–62. <https://doi.org/10.2118/942054-G>
- Avellaneda, M., & Torquato, S. (1991). Rigorous link between fluid permeability, electrical conductivity, and relaxation times for transport in porous media. *Physics of Fluids A: Fluid Dynamics*, *3*(11), 2529–2540. <https://doi.org/10.1063/1.858194>
- Banavar, J. R., & Johnson, D. L. (1987). Characteristic pore sizes and transport in porous media. *Physical Review B*, *35*(13), 7283–7286. <https://doi.org/10.1103/PhysRevB.35.7283>
- Behroozmand, A. A., Keating, K., & Auken, E. (2015). A review of the principles and applications of the NMR technique for near-surface characterization. *Surveys in Geophysics*, *36*(1), 27–85. <https://doi.org/10.1007/s10712-014-9304-0>
- Bernabé, Y., Li, M., & Maeneult, A. (2010). Permeability and pore connectivity: A new model based on network simulations. *Journal of Geophysical Research*, *115*, B10203. <https://doi.org/10.1029/2010JB007444>
- Bernabé, Y., Mok, U., & Evans, B. (2003). Permeability-porosity relationships in rocks subjected to various evolution processes. *Pure and Applied Geophysics*, *160*(5), 937–960. <https://doi.org/10.1007/PL00012574>
- Bernard, M. L., Zamora, M., Géraud, Y., & Boudon, G. (2007). Transport properties of pyroclastic rocks from Montagne Pelée volcano (Martinique, Lesser Antilles). *Journal of Geophysical Research*, *112*, B05205. <https://doi.org/10.1029/2006JB004385>
- Binley, A., Hubbard, S. S., Huisman, J. A., Revil, A., Robinson, D. A., Singha, K., & Slater, L. D. (2015). The emergence of hydrogeophysics for improved understanding of subsurface processes over multiple scales. *Water Resources Research*, *51*, 3837–3866. <https://doi.org/10.1002/2015WR017016>
- Binley, A., Slater, L. D., Fukes, M., & Cassiani, G. (2005). Relationship between spectral induced polarization and hydraulic properties of saturated and unsaturated sandstone. *Water Resources Research*, *41*, W12417. <https://doi.org/10.1029/2005WR004202>
- Blunt, M. J., Bijeljic, B., Dong, H., Gharbi, O., Iglauer, S., Mostaghimi, P., et al. (2013). Pore-scale imaging and modelling. *Advances in Water Resources*, *51*, 197–216. <https://doi.org/10.1016/j.advwatres.2012.03.003>
- Borgia, G. C., Brown, R. J. S., & Fantazzini, P. (1996). Nuclear magnetic resonance relaxivity and surface-to-volume ratio in porous media with a wide distribution of pore sizes. *Journal of Applied Physics*, *79*(7), 3656–3664. <https://doi.org/10.1063/1.361194>
- Börner, F. D. (1992). Complex conductivity measurements of reservoir properties. Paper presented at Proceedings of the Third European Core Analysis Symposium.
- Bourbie, T., & Zinszner, B. (1985). Hydraulic and acoustic properties as a function of porosity in Fontainebleau sandstone. *Journal of Geophysical Research*, *90*(B13), 11,524–11,532. <https://doi.org/10.1029/JB090iB13p11524>
- Brace, W. F. (1980). Permeability of crystalline and argillaceous rocks. *International Journal of Rock Mechanics and Mining Sciences & Geomechanics Abstracts*, *17*(5), 241–251. [https://doi.org/10.1016/0148-9062\(80\)90807-4](https://doi.org/10.1016/0148-9062(80)90807-4)
- Bryant, S., & Blunt, M. (1992). Prediction of relative permeability in simple porous media. *Physical Review A*, *46*(4), 2004–2011. <https://doi.org/10.1103/PhysRevA.46.2004>
- Burdine, N. (1953). Relative permeability calculations from pore size distribution data. *Journal of Petroleum Technology*, *5*(03), 71–78. <https://doi.org/10.2118/225-G>
- Cai, J., Perfect, E., Cheng, C.-L., & Hu, X. (2014). Generalized modeling of spontaneous imbibition based on Hagen–Poiseuille flow in tortuous capillaries with variably shaped apertures. *Langmuir*, *30*(18), 5142–5151. <https://doi.org/10.1021/la5007204>

- Cardell, C., Benavente, D., & Rodriguez-Gordillo, J. (2008). Weathering of limestone building material by mixed sulfate solutions. Characterization of stone microstructure, reaction products and decay forms. *Materials Characterization*, 59(10), 1371–1385.
- Carman, P. C. (1937). Fluid flow through granular beds. *Transactions Institute of Chemical Engineers*, 15, 150–166.
- Daigle, H., & Dugan, B. (2011). An improved technique for computing permeability from NMR measurements in mudstones. *Journal of Geophysical Research*, 116, B08101. <https://doi.org/10.1029/2011JB008353>
- Dong, H., & Blunt, M. J. (2009). Pore-network extraction from micro-computerized-tomography images. *Physical Review E*, 80(3), 036307. <https://doi.org/10.1103/PhysRevE.80.036307>
- Duda, A., Koza, Z., & Matyka, M. (2011). Hydraulic tortuosity in arbitrary porous media flow. *Physical Review E*, 84(3), 036319. <https://doi.org/10.1103/PhysRevE.84.036319>
- Ehrenberg, S. N., & Nadeau, P. H. (2005). Sandstone vs. carbonate petroleum reservoirs: A global perspective on porosity-depth and porosity-permeability relationships. *AAPG bulletin*, 89(4), 435–445. <https://doi.org/10.1306/11230404071>
- Emberley, S., Hutcheon, I., Shevalier, M., Durocher, K., Gunter, W. D., & Perkins, E. H. (2004). Geochemical monitoring of fluid-rock interaction and CO<sub>2</sub> storage at the Weyburn CO<sub>2</sub>-injection enhanced oil recovery site, Saskatchewan, Canada. *Energy*, 29(9–10), 1393–1401. <https://doi.org/10.1016/j.energy.2004.03.073>
- Fredlund, D. G., Xing, A. Q., & Huang, S. Y. (1994). Predicting the permeability function for unsaturated soils using the soil-water characteristic curve. *Canadian Geotechnical Journal*, 31(4), 533–546. <https://doi.org/10.1139/t94-062>
- Friesen, O. J., Dashtgard, S. E., Miller, J., Schmitt, L., & Baldwin, C. (2017). Permeability heterogeneity in bioturbated sediments and implications for waterflooding of tight-oil reservoirs, Cardium Formation, Pembina Field, Alberta, Canada. *Marine and Petroleum Geology*, 82, 371–387. <https://doi.org/10.1016/j.marpetgeo.2017.01.019>
- Garboczi, E. J. (1990). Permeability, diffusivity, and microstructural parameters: A critical review. *Cement and Concrete Research*, 20(4), 591–601. [https://doi.org/10.1016/0008-8846\(90\)90101-3](https://doi.org/10.1016/0008-8846(90)90101-3)
- Garboczi, E. J. (1998). Finite element and finite difference programs for computing the linear electric and elastic properties of digital images of random materials.
- Garcia-Rios, M., Luquot, L., Soler, J. M., & Cama, J. (2015). Influence of the flow rate on dissolution and precipitation features during percolation of CO<sub>2</sub>-rich sulfate solutions through fractured limestone samples. *Chemical Geology*, 414, 95–108. <https://doi.org/10.1016/j.chemgeo.2015.09.005>
- Ghezzehei, T. A. (2012). Linking sub-pore scale heterogeneity of biological and geochemical deposits with changes in permeability. *Advances in Water Resources*, 39, 1–6. <https://doi.org/10.1016/j.advwatres.2011.12.015>
- Golfier, F., Zarcone, C., Bazin, B., Lenormand, R., Lasseux, D., & Quintard, M. (2002). On the ability of a Darcy-scale model to capture wormhole formation during the dissolution of a porous medium. *Journal of Fluid Mechanics*, 457, 213–254.
- Gomez, C. T., Dvorkin, J., & Vanorio, T. (2010). Laboratory measurements of porosity, permeability, resistivity, and velocity on Fontainebleau sandstones. *Geophysics*, 75(6), E191–E204. <https://doi.org/10.1190/1.3493633>
- Honarpour, M., Cullick, A., Saad, N., & Humphreys, N. (1995). Effect of rock heterogeneity on relative permeability: Implications for scale-up. *Journal of Petroleum Technology*, 47(11), 980–986. <https://doi.org/10.2118/29311-PA>
- Jiang, F., & Tsuji, T. (2014). Changes in pore geometry and relative permeability caused by carbonate precipitation in porous media. *Physical Review E*, 90(5), 053306. <https://doi.org/10.1103/PhysRevE.90.053306>
- Johnson, D. L., Koplik, J., & Schwartz, L. M. (1986). New pore-size parameter characterizing transport in porous media. *Physical Review Letters*, 57(20), 2564–2567. <https://doi.org/10.1103/PhysRevLett.57.2564>
- Kang, Q., Zhang, D., & Chen, S. (2003). Simulation of dissolution and precipitation in porous media. *Journal of Geophysical Research*, 108(B10), 2505. <https://doi.org/10.1029/2003JB002504>
- Katz, A. J., & Thompson, A. H. (1986). Quantitative prediction of permeability in porous rock. *Physical Review B*, 34(11), 8179–8181. <https://doi.org/10.1103/PhysRevB.34.8179>
- Kelemen, P. B., Whitehead, J. A., Aharonov, E., & Jordahl, K. A. (1995). Experiments on flow focusing in soluble porous media, with applications to melt extraction from the mantle. *Journal of Geophysical Research*, 100(B1), 475–496. <https://doi.org/10.1029/94JB02544>
- Kenyon, W. E., Day, P. I., Straley, C., & Willemsen, J. F. (1988). A three-part study of NMR longitudinal relaxation properties of water-saturated sandstones. *SPE Formation Evaluation*, 3(03), 622–636. <https://doi.org/10.2118/15643-PA>
- Kostek, S., Schwartz, L. M., & Johnson, D. L. (1992). Fluid permeability in porous media: Comparison of electrical estimates with hydrodynamical calculations. *Physical Review B*, 45(1), 186–195. <https://doi.org/10.1103/PhysRevB.45.186>
- Kosugi, K. (1996). Lognormal distribution model for unsaturated soil hydraulic properties. *Water Resources Research*, 32(9), 2697–2703. <https://doi.org/10.1029/96WR01776>
- Kwon, O., Kronenberg, A. K., Gangi, A. F., Johnson, B., & Herbert, B. E. (2004). Permeability of illite-bearing shale: 1. Anisotropy and effects of clay content and loading. *Journal of Geophysical Research*, 109, B10205. <https://doi.org/10.1029/2004JB003052>
- Leroy, P., Li, S., Jougnot, D., Revil, A., & Wu, Y. (2017). Modelling the evolution of complex conductivity during calcite precipitation on glass beads. *Geophysical Journal International*, 209(1), 123–140.
- Lindquist, W. B., Lee, S. M., Coker, D. A., Jones, K. W., & Spanne, P. (1996). Medial axis analysis of void structure in three-dimensional tomographic images of porous media. *Journal of Geophysical Research*, 101(B4), 8297–8310. <https://doi.org/10.1029/95JB03039>
- Lindquist, W. B., Venkatarangan, A., Dunsmuir, J., & Wong, T.-f. (2000). Pore and throat size distributions measured from synchrotron X-ray tomographic images of Fontainebleau sandstones. *Journal of Geophysical Research*, 105(B9), 21,509–21,527. <https://doi.org/10.1029/2000JB900208>
- Lu, N., & Likos, W. J. (2004). *Unsaturated soil mechanics*. New York: John Wiley.
- Luhmann, A. J., Tutolo, B. M., Bagley, B. C., Mildner, D. F. R., Seyfried, W. E., & Saar, M. O. (2017). Permeability, porosity, and mineral surface area changes in basalt cores induced by reactive transport of CO<sub>2</sub>-rich brine. *Water Resources Research*, 53, 1908–1927. <https://doi.org/10.1002/2016WR019216>
- Luquot, L., & Gouze, P. (2009). Experimental determination of porosity and permeability changes induced by injection of CO<sub>2</sub> into carbonate rocks. *Chemical Geology*, 265(1–2), 148–159. <https://doi.org/10.1016/j.chemgeo.2009.03.028>
- Maurya, P. K., Balbarini, N., Møller, I., Ronde, V., Christiansen, A. V., Bjerg, P. L., et al. (2018). Subsurface imaging of water electrical conductivity, hydraulic permeability and lithology at contaminated sites by induced polarization. *Geophysical Journal International*, 213(2), 770–785. <https://doi.org/10.1093/gji/ggy018>
- Miller, K., Vanorio, T., & Keehm, Y. (2017). Evolution of permeability and microstructure of tight carbonates due to numerical simulation of calcite dissolution. *Journal of Geophysical Research: Solid Earth*, 122, 4460–4474. <https://doi.org/10.1002/2017JB013972>
- Molins, S., Trebotich, D., Miller, G. H., & Steefel, C. I. (2017). Mineralogical and transport controls on the evolution of porous media texture using direct numerical simulation. *Water Resources Research*, 53, 3645–3661. <https://doi.org/10.1002/2016WR020323>

- Montoya, B. M., & DeJong, J. T. (2015). Stress-strain behavior of sands cemented by microbially induced calcite precipitation. *Journal of Geotechnical and Geoenvironmental Engineering*, *141*(6), 04015019. [https://doi.org/10.1061/\(ASCE\)GT.1943-5606.0001302](https://doi.org/10.1061/(ASCE)GT.1943-5606.0001302)
- Morse, J. W., Arvidson, R. S., & Lüttge, A. (2007). Calcium carbonate formation and dissolution. *Chemical Reviews*, *107*(2), 342–381. <https://doi.org/10.1021/cr050358j>
- Mualem, Y. (1976). A new model for predicting the hydraulic conductivity of unsaturated porous media. *Water Resources Research*, *12*(3), 513–522. <https://doi.org/10.1029/WR012i003p00513>
- Niu, Q., Fratta, D., & Wang, Y.-H. (2015). The use of electrical conductivity measurements in the prediction of hydraulic conductivity of unsaturated soils. *Journal of Hydrology*, *522*, 475–487. <https://doi.org/10.1016/j.jhydrol.2014.12.055>
- Niu, Q., & Zhang, C. (2017). Pore-scale modelling of complex conductivity of saturated granular materials. *Near Surface Geophysics*, *15*(6), 593–602.
- Niu, Q., & Zhang, C. (2018). Physical explanation of Archie's porosity exponent in granular materials: A process-based, pore-scale numerical study. *Geophysical Research Letters*, *45*, 1870–1877. <https://doi.org/10.1002/2017GL076751>
- Noiriel, C. (2015). Resolving time-dependent evolution of pore-scale structure, permeability and reactivity using X-ray microtomography. *Reviews in Mineralogy and Geochemistry*, *80*(1), 247–285. <https://doi.org/10.2138/rmg.2015.80.08>
- Noiriel, C., Gouze, P., & Bernard, D. (2004). Investigation of porosity and permeability effects from microstructure changes during limestone dissolution. *Geophysical Research Letters*, *31*, L24603. <https://doi.org/10.1029/2004GL021572>
- Noiriel, C., Steefel, C. I., Yang, L., & Bernard, D. (2016). Effects of pore-scale precipitation on permeability and flow. *Advances in Water Resources*, *95*, 125–137. <https://doi.org/10.1016/j.advwatres.2015.11.013>
- Nunes, J. P. P., Blunt, M. J., & Bijeljic, B. (2016). Pore-scale simulation of carbonate dissolution in micro-CT images. *Journal of Geophysical Research: Solid Earth*, *121*, 558–576. <https://doi.org/10.1002/2015JB012117>
- Ott, H., & Oedai, S. (2015). Wormhole formation and compact dissolution in single- and two-phase CO<sub>2</sub>-brine injections. *Geophysical Research Letters*, *42*, 2270–2276. <https://doi.org/10.1002/2015GL063582>
- Paniconi, C., & Putti, M. (2015). Physically based modeling in catchment hydrology at 50: Survey and outlook. *Water Resources Research*, *51*, 7090–7129. <https://doi.org/10.1002/2015WR017780>
- Popp, T., Kern, H., & Schulze, O. (2001). Evolution of dilatancy and permeability in rock salt during hydrostatic compaction and triaxial deformation. *Journal of Geophysical Research*, *106*(B3), 4061–4078. <https://doi.org/10.1029/2000JB900381>
- Qin, C.-Z., Hassanizadeh, S. M., & Ebigbo, A. (2016). Pore-scale network modeling of microbially induced calcium carbonate precipitation: Insight into scale dependence of biogeochemical reaction rates. *Water Resources Research*, *52*, 8794–8810. <https://doi.org/10.1002/2016WR019128>
- Revil, A., Binley, A., Mejus, L., & Kessouri, P. (2015). Predicting permeability from the characteristic relaxation time and intrinsic formation factor of complex conductivity spectra. *Water Resources Research*, *51*, 6672–6700. <https://doi.org/10.1002/2015WR017074>
- Revil, A., & Cathles, L. M. (1999). Permeability of shaly sands. *Water Resources Research*, *35*(3), 651–662. <https://doi.org/10.1029/98WR02700>
- Revil, A., & Florsch, N. (2010). Determination of permeability from spectral induced polarization in granular media. *Geophysical Journal International*, *181*(3), 1480–1498.
- Revil, A., & Glover, P. W. J. (1998). Nature of surface electrical conductivity in natural sands, sandstones, and clays. *Geophysical Research Letters*, *25*(5), 691–694. <https://doi.org/10.1029/98GL00296>
- Revil, A., Kessouri, P., & Torres-Verdin, C. (2014). Electrical conductivity, induced polarization, and permeability of the Fontainebleau sandstone. *Geophysics*, *79*(5), D301–D318. <https://doi.org/10.1190/geo2014-0036.1>
- Rizzo, C. B., & de Barros, F. P. J. (2017). Minimum hydraulic resistance and least resistance path in heterogeneous porous media. *Water Resources Research*, *53*, 8596–8613. <https://doi.org/10.1002/2017WR020418>
- Schuh, W., & Cline, R. (1990). Effect of soil properties on unsaturated hydraulic conductivity pore-interaction factors. *Soil Science Society of America Journal*, *54*(6), 1509–1519. <https://doi.org/10.2136/sssaj1990.03615995005400060001x>
- Schwartz, L. M., Sen, P. N., & Johnson, D. L. (1989). Influence of rough surfaces on electrolytic conduction in porous media. *Physical Review B*, *40*(4), 2450–2458. <https://doi.org/10.1103/PhysRevB.40.2450>
- Slater, L., & Lesmes, D. P. (2002). Electrical-hydraulic relationships observed for unconsolidated sediments. *Water Resources Research*, *38*(10), 1213. <https://doi.org/10.1029/2001WR001075>
- Steeffel, C. I., & Lasaga, A. C. (1994). A coupled model for transport of multiple chemical species and kinetic precipitation/dissolution reactions with application to reactive flow in single phase hydrothermal systems. *American Journal of Science*, *294*(5), 529–592. <https://doi.org/10.2475/ajs.294.5.529>
- Torquato, S. (2002). *Random heterogeneous materials: microstructure and macroscopic properties*. New York: Springer Science & Business Media.
- Weller, A., Breede, K., Slater, L., & Nordsiek, S. (2011). Effect of changing water salinity on complex conductivity spectra of sandstones. *Geophysics*, *76*(5), F315–F327. <https://doi.org/10.1190/geo2011-0072.1>
- Weller, A., & Slater, L. (2015). Induced polarization dependence on pore space geometry: Empirical observations and mechanistic predictions. *Journal of Applied Geophysics*, *123*, 310–315. <https://doi.org/10.1016/j.jappgeo.2015.09.002>
- Weller, A., Slater, L., Binley, A., Nordsiek, S., & Xu, S. (2015). Permeability prediction based on induced polarization: Insights from measurements on sandstone and unconsolidated samples spanning a wide permeability range. *Geophysics*, *80*(2), D161–D173. <https://doi.org/10.1190/geo2014-0368.1>
- Whitaker, F. F., & Smart, P. L. (1997). Groundwater circulation and geochemistry of a karstified bank–marginal fracture system, South Andros Island, Bahamas. *Journal of Hydrology*, *197*(1–4), 293–315. [https://doi.org/10.1016/S0022-1694\(96\)03274-X](https://doi.org/10.1016/S0022-1694(96)03274-X)
- Wildenschild, D., & Sheppard, A. P. (2013). X-ray imaging and analysis techniques for quantifying pore-scale structure and processes in subsurface porous medium systems. *Advances in Water Resources*, *51*, 217–246. <https://doi.org/10.1016/j.advwatres.2012.07.018>
- Xu, P., & Yu, B. (2008). Developing a new form of permeability and Kozeny–Carman constant for homogeneous porous media by means of fractal geometry. *Advances in Water Resources*, *31*(1), 74–81. <https://doi.org/10.1016/j.advwatres.2007.06.003>
- Yoon, H., Valocchi, A. J., Werth, C. J., & Dewers, T. (2012). Pore-scale simulation of mixing-induced calcium carbonate precipitation and dissolution in a microfluidic pore network. *Water Resources Research*, *48*, W02524. <https://doi.org/10.1029/2011WR011192>
- Zhan, X., Schwartz, L. M., Toksöz, M. N., Smith, W. C., & Morgan, F. D. (2010). Pore-scale modeling of electrical and fluid transport in Berea sandstone. *Geophysics*, *75*(5), F135–F142. <https://doi.org/10.1190/1.3463704>
- Zhu, W., Tivey, M. K., Gittings, H., & Craddock, P. R. (2007). Permeability-porosity relationships in seafloor vent deposits: Dependence on pore evolution processes. *Journal of Geophysical Research*, *112*, B05208. <https://doi.org/10.1029/2006JB004716>